Editors' Suggestion

Ferroelectric nanodomains in epitaxial GeTe thin films

Boris Croes,[1] Fabien Cheynis,[1] Yide Zhang,[2] Cédric Voulot,[2] Kokou Dodzi Dorkenoo,[2] Salia Cherifi-Hertel,[2] Cristian Mocuta,[3] Michaël Texier,[4] Thomas Cornelius,[4] Olivier Thomas,[4] Marie-Ingrid Richard,[5] Pierre Müller,[1] Stefano Curiotto,[1] and Frédéric Leroy[1,*]

[1]*Aix Marseille Université, CNRS, CINAM, AMUTECH, Marseille, France*
[2]*Université de Strasbourg, CNRS, Institut de Physique et Chimie des Matériaux de Strasbourg, Strasbourg 67000, France*
[3]*Synchrotron SOLEIL, L'Orme des Merisiers, St Aubin BP 48, F-91192 Gif Sur Yvette, France*
[4]*Aix Marseille Université, Université Toulon, IM2NP, AMUTECH, CNRS, F-13397 Marseille 20, France*
[5]*Université Grenoble Alpes, CEA Grenoble, IRIG, MEM,NRS, 17 Rue Martyrs, F-38000 Grenoble, France*

(Received 29 July 2021; accepted 2 December 2021; published 23 December 2021)

In the quest for materials for ferroelectrics-based spintronics with a large spin-orbit coupling, it is essential to carefully control the ferroelectric domains structure, their spatial organization, and the domain wall type. Here we perform the growth of GeTe thin films on Si by molecular beam epitaxy in a large thickness range. We show that the volume fraction along with the size of the ferroelectric nanodomains can be controlled by finely adjusting the deposition thickness and temperature. We evidence that the formation of 71°-type domain walls and *in situ* measurements during thermal cycling show the hysteretic appearance and decay of ferroelectric domains. In combination with a detailed analysis of the GeTe/Si interface, we demonstrate that the interfacial misfit dislocations formed during the growth play a key role in the stability of the ferroelectric nanodomains.

DOI: 10.1103/PhysRevMaterials.5.124415

I. INTRODUCTION

The epitaxial growth of thin films on single crystal substrates often leads to the development of strain fields. In ferroelectrics, this provides an extra degree of freedom to control their structure, ferroelectric transition temperature, and related functionalities such as optical, dielectric, and piezoelectric responses [1–3]. The domain structure plays a central role in the relaxation mechanisms, owing to its strong dependence on tensile or compressive strain that is imposed by the substrate. Recently, strain engineering, by the selection of appropriate substrates, and the control of charge screening in thin films and superlattices, has led to the discovery of new ferroelectric phases showing exotic domain patterns and polarization textures [4–8]. Furthermore, strain relaxation in thick films is often accompanied by the formation of ferroelastic domains and twin boundaries which can add further functionalization [9] via self-organized domain patterns [10–12].

Among ferroelectrics a new class of materials with high potentialities for spintronic applications has recently been introduced as ferroelectric Rashba semiconductors (FERSCs) [13,14]. Main results, obtained on α-GeTe thin films, have demonstrated that the reversal of the ferroelectric polarization under an electric field leads to a consistent change in the spin chirality of the band structure [15,16]. An effective spin-to-charge conversion has also been demonstrated in a ferromagnetic-GeTe heterostructure [17,18] and a nonreciprocal charge transport up to room temperature has been detected [19]. All these advances pave the way for an all-electric spintronics based on semiconducting materials. However, the influence of the domain structure on these phenomena still remains unclear. Given the rhombohedral structure of GeTe ($R3m$ space group) and the existence of an electric dipole in the $\langle 111 \rangle$ direction, eight possible polar domain orientations are anticipated in this system. This was unambiguously confirmed by the observation of herringbone domain configurations in low-temperature α-phase GeTe crystals [20,21]. In the context of epitaxial (111)-oriented thin films a dominant self-poled state with a polarization perpendicular to the surface has been evidenced [15,16,22]. However a few results [23,24] indicate that this is a simplified view and minority incursions occur in thin films. In spite of the growing interest in such ferroelectric Rashba semiconductors [25,26], the detailed polar domain structure and spatial organization has not been studied so far. These studies are a prerequisite for the controlled switching of ferroelectric domains and the understanding of aging properties.

In this article we address the ferroelectric nanodomains organization of α-GeTe thin films grown on Si(111), the domain wall type, and the structure of the interface with the substrate. As reported by Wang *et al.* [23], quasisingle crystalline α-GeTe thin films can be grown on Si(111) by molecular beam epitaxy using a predeposition of 1 monolayer (ML) of Sb onto the substrate. It is an ideal platform to study and control ferroelectric domains as they are no longer limited by grain boundaries. We have determined by x-ray diffraction (three-dimensional reciprocal space maps) in combination with low energy electron microscopy (LEEM) the volume fraction of the ferroelectric domains and the domains size in a large range of film thickness (10–1800 nm). Second harmonic generation

*leroy@cinam.univ-mrs.fr

 ©2021 American Physical Society

(SHG) microscopy combined with polarimetry analysis reveal the local symmetry of these domains. Using high resolution transmission electron microscopy (HR-TEM) we show that domain walls are only of 71° type and that the GeTe/Si interface is stabilized by misfit dislocations that relax the large lattice parameter mismatch between both lattices. The reversible decay/growth of the ferroelectric nanodomains under annealing/cooling, as demonstrated by *in situ* LEEM, is attributed to the thermal stress induced by the large difference of linear thermal expansion coefficients of both materials.

II. METHODS

A. Sample preparation and GeTe thin film growth by molecular beam epitaxy

Si(111) wafers (Siltronix: 550-μm-thick; $\rho = 1$–$10\ \Omega\,\text{cm}$) are first cleaned by acetone and ethanol rinsing before introduction in ultrahigh vacuum (UHV, $P < 10^{-7}$ Pa). Then the substrates are degassed at 1000 K during 12 h followed by repeated high temperature annealing (1500 K) during a few minutes in order to achieve a clean 7×7 surface reconstruction. Finally, a deposition of 1 ML of Sb is performed on the Si(111) surface, forming the so-called Si(111)-$\sqrt{3} \times \sqrt{3}$-Sb reconstruction [27] that greatly improves the crystalline quality of the GeTe layer [23]. The GeTe thin films are grown by co-deposition of Ge (1100 °C) and Te (310 °C) in UHV at 275 °C and characterized by *in situ* reflection high energy electron diffraction (RHEED). All the deposition sources are effusion cells from MBE-Komponenten Gmbh.

B. LEEM and LEED surface characterization of nanodomains

After growth the GeTe layers are transferred under UHV conditions and characterized by low energy electron microscopy and low energy electron diffraction (LEEM III, Elmitec GmbH). LEEM images were obtained in bright field mode at an incident energy of 26 eV where a local maximum of reflectivity occurs. At this energy the reflected beams by the GeTe main domain and by the tilted ferroelectric nanodomains are clearly separated in the focal plane. This allows us to use either the medium contrast aperture ($\varnothing = 30\ \mu$m) to select all reflected beams or the smallest contrast aperture ($\varnothing = 10\ \mu$m) to select only the reflected beam from the main domain. *In situ* LEEM characterization of the domains evolution under thermal treatments were performed with temperature steps of 10 °C and waiting time of 30 min for stabilization.

C. X-ray diffraction and 3D reciprocal space maps

The internal structure of GeTe thin films has been studied by x-ray diffraction at DiffAbs beamline (Synchrotron SOLEIL). X-ray diffraction data have been measured at 9.5 keV (0.13051 nm) and 16.9 keV (0.07336 nm). The incident beam was focused on the sample surface to a size of $250 \times 300\ \mu\text{m}^2$. The diffracted intensity was collected onto a two-dimensional (2D) XPAD hybrid pixel detector. Three-dimensional (3D) reciprocal space maps of the GeTe 222_c Bragg reflection were recorded by rocking the sample by ±3°. The typical step was about 0.01°. The data analysis consists of a flat field correction (of the possible nonuniform response of the various pixels of the detector) and then a conversion of the measured data from the detector coordinates (pixel index) to diffraction angles and thus to reciprocal space [28]. The 3D reciprocal space map have been visualized finally using the ParaView software.

D. High-resolution transmission electron microscopy

HR-TEM investigations were performed with $[1\bar{1}0]$ zone axis at an accelerating voltage of 300 kV on a JEOL JEM-3010 instrument with a spatial resolution of 0.17 nm. Using a focused ion beam preparation procedure (Dual beam FIB, FEI Helios 600 NanoLab), electron transparent ultrathin sections were extracted from the thin films of GeTe on Si. The typical dimensions of the electron transparent ultrathin sections are 15 μm (length) × 5 μm (height) × 150–200 nm (thickness). Geometric phase analysis (GPA) was performed using the strain++ software applying a mask in reciprocal space of radius 0.8 nm^{-1} producing a lateral resolution in the images of 1.25 nm.

E. Second harmonic generation microscopy and polarimetry analysis

Local SHG measurements were conducted by means of an inverted optical microscope. The fundamental wave is provided by a laser source emitting pulses of 100 fs duration at a repetition rate of 80 MHz, centered at a wavelength $\lambda = 800$ nm. The sample was illuminated at normal incidence with a time-averaged power of 11 mW. The SHG images are obtained by scanning the sample with respect to the focused laser beam [objective ×60, 0.85 numerical aperture (NA)] using computer-controlled stepping motors. The output intensity was spectrally filtered and collected into a photomultiplier. Polarimetry measurements are performed by recording the SHG images at different polarizer and analyzer angles. In the case of a medium focusing of the fundamental beam (0.70 NA, or smaller), a scalar model using the analytic form of SHG is sufficient to model the local polarimetry response at polar domains [29], domain walls [30–32]. The use of a strong focusing (0.85 NA) was necessary in this study to properly resolve the fine ferroelastic needles. In this case a vectorial treatment of the fundamental electric field is necessary [33,34]. We have thus developed a semianalytic model for the second harmonic polarimetry, combining the analytic form of SHG with a vectorial modeling of the fundamental focused electric field [36]. The as derived fitting functions also take into account the mixed character of the studied volumes (containing both a- and c-domain fractions) in both polarization plots (P plots) and anisotropy plots (simultaneous rotation of the polarization and analyzer). The fitting functions related to both measurement geometries are presented in the Supplemental Material (Note 1) [35].

III. RESULTS AND DISCUSSION

In order to determine the structure of GeTe thin films, we have performed x-ray diffraction measurements. In Fig. 1(a), the iso-intensity surfaces of 3D reciprocal space maps [37] of GeTe epitaxial thin films close to 222_c show four Bragg

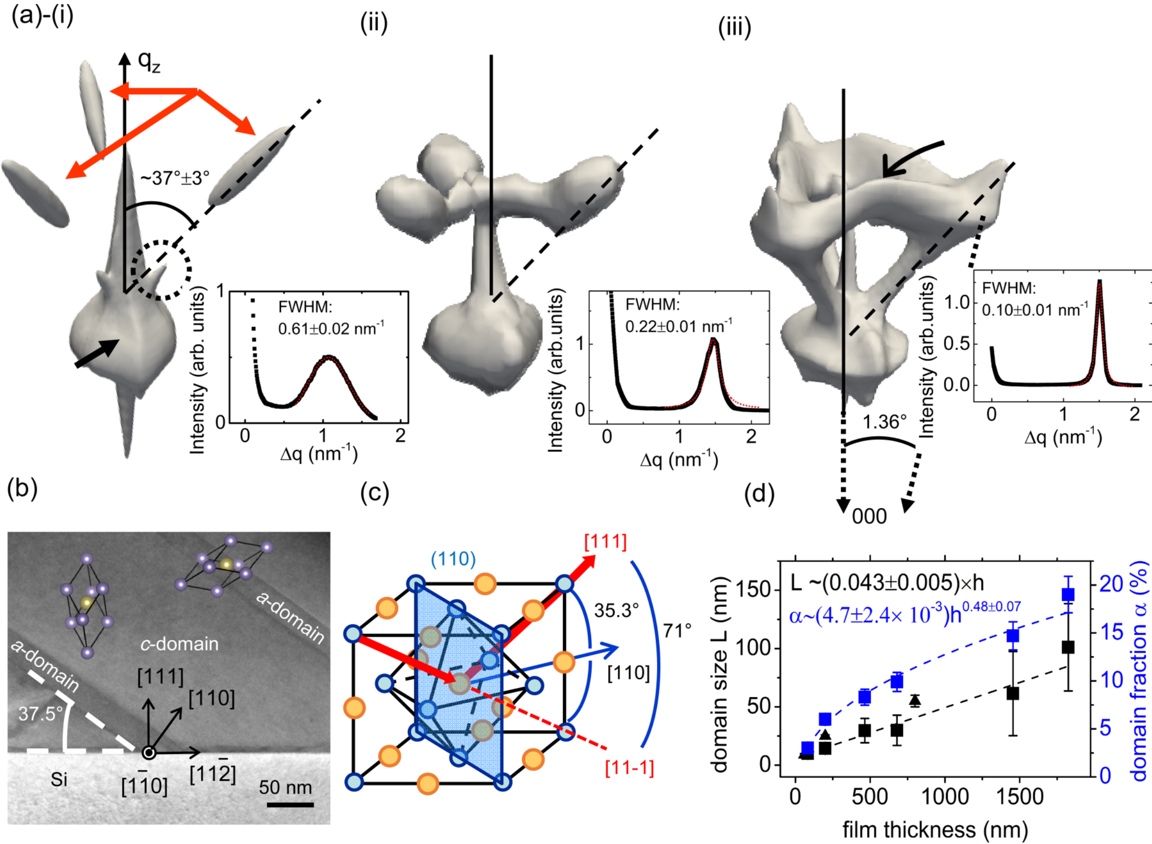

FIG. 1. (a)–(i) Iso-intensity surface (2500 counts) of a 3D reciprocal space map around 222_c Bragg peak of a 60-nm-thick GeTe thin film. Bragg peaks of main GeTe *c* domains (black arrow) and ferroelastic *a* nanodomains (red arrows). Minor ferroelastic Bragg peaks from the *a* nanodomains are elongated at $\sim 37^\circ \pm 3^\circ$ with respect to q_z axis (line profile along the dashed line in inset). Similar elongation of the diffuse scattering of GeTe *c* domain (dotted circle) arising from the truncation of the *c* domains by inclined *a* domains (Babinet principle). (ii) and (iii) Same as (i) for a 200 nm (5000 counts) and 800-nm-thick (3000 counts) GeTe thin film. X-ray diffuse scattering bridge due to domains intersection (curved black arrow). (b) TEM cross section of a 460-nm-thick GeTe thin film with medium resolution showing two *a* nanodomains crossing the film ([1$\bar{1}$0] zone axis). The rhombohedral unit cells indicates the elongation direction of the domains. (c) Scheme of the polarization (rhombohedral elongation) of the main GeTe *c* domains along [111] and a secondary ferroelastic *a* domain along [11$\bar{1}$] (in pseudocubic representation). (d) Domain size *L* and volume fraction *α* of ferroelastic domains in GeTe thin films as a function of film thickness deduced from the full-width at half-maximum of diffraction peaks of ferroelastic domains (triangle) and LEEM measurements (square).

peaks (*c* stands for a pseudocubic unit cell). The main Bragg peak is located along the axis perpendicular to the surface and is centered at $q_z = 35.408 \pm 0.010$ nm^{-1}. This Bragg peak position at low q_z can be assigned to a rhombohedral distortion of GeTe thin films stretched along the [111] growth axis. In the following the real space regions giving rise to this Bragg peak are referred to as *c* domains that constitute the vast majority of the thin film. In addition, three minor Bragg peaks are slightly angularly offset from this axis and localized at higher $q_z = 36.733 \pm 0.010$ nm^{-1}. They can be assigned to minor ferroelastic domains with a rhombohedral distortion along [11$\bar{1}$, [1$\bar{1}$1], and [$\bar{1}$11] (labeled *a* domains). These distortions induce a rotation of the (111) crystallographic planes by $1.36^\circ \pm 0.04^\circ$ [see Fig. 1(a)-(iii)] and a slight compression of the (111) inter-reticular distance of 3.74% with respect to *c* domains.

To determine the domain boundary type, the x-ray diffuse scattering around Bragg peaks provides some hints. The minor Bragg peaks from the ferroelastic *a* domains are clearly elongated along a precise direction in reciprocal space ($37^\circ \pm 3^\circ$ with respect to q_z axis) and this extension is more pronounced for thinner films (60-nm-thick GeTe thin film). This diffuse scattering indicates the presence of well defined interfaces between *a* and *c* domains and can be assigned to 71°-type domain walls due to finite size effect along the [110] direction [Fig. 1(c)]. TEM cross-section views [Fig. 1(b)] show indeed that ferroelastic *a* domains are crossing the film with sharp and straight walls perpendicular to the [110] direction. These sharp interfaces are the only one observed between the *c* domains and *a* domains. For the thinnest films [Figs. 1(a)–1(i)], no additional x-ray diffuse scattering is measured, indicating that ferroelastic *a* domains are independent and do not intersect each other. For thicker films, the volume fraction of ferroelastic *a* domains increases as shown by the increase of the ratio of the integrated intensities of minor Bragg peaks with respect to the major peak [Fig. 1(d)]. This gives rise also to a more complex diffuse scattering pattern originating from the intersection area between ferroelastic *a* domains of different variants. Experimental signatures of these intersections arise from diffuse scattering bridge patterns [37,38] localized

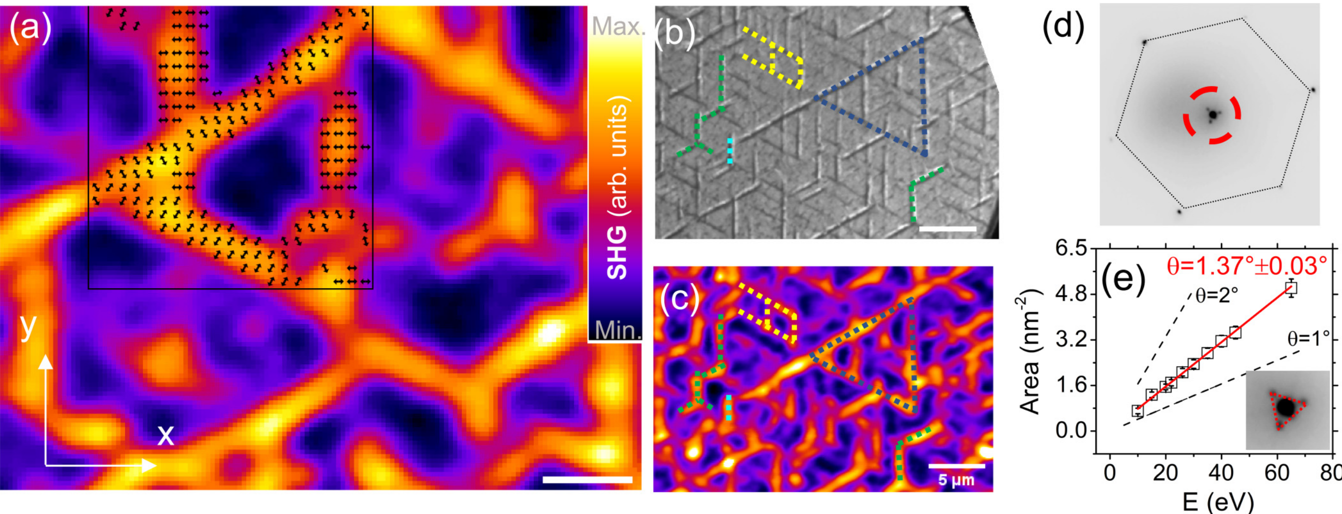

FIG. 2. (a) Isotropic second harmonic image revealing the domain structure of a 1825-nm-thick GeTe film. The black arrows indicate the local in-plane polarization orientation in the nanodomains as derived from pixel-by-pixel polarimetry analysis (see the Supplemental Material, Fig. S3 [35]). The three different a domain contributions (at -30°, 30°, and 90° with respect to x axis) are superimposed to the background (dark purple) signal exhibiting out-of-plane polarization (c domain). The scale bar corresponds to 2 μm. (b) LEEM image (bright field mode, incident electron energy: 26 eV) from the GeTe thin film (scale bar 5 μm). (c) Same area visualized by spatially resolved SHG. Dashed lines in (b) and (c) are markers. (d) μ-LEED pattern (20 μm incident beam size) at 26 eV incident electron energy showing four reflected beams inside a red dot circle: a main reflected beam and three minor beams originating from the nanodomains. (e) Area of the triangle formed by the three reflected beams (nanodomains) as a function of the incident electron energy (from 8 to 65 eV). Linear fit (red line) and simulations for different tilt angles (dashed lines).

between ferroelastic a nanodomain Bragg peaks [Fig. 1(a)-(iii)]. The center of mass of the bridges indicates a 60° in-plane rotation of the strain, a tilt angle of $0.79^{\circ} \pm 0.05^{\circ}$, and an increased compression of the (111) crystallographic planes by 4.37% in the intersection area ($q_z = 36.954 \pm 0.010\ \mathrm{nm}^{-1}$). Complementary x-ray diffraction measurements on nonsymmetric Bragg peaks show that all the domains have a rhombohedral structure ($a = 0.429$ nm, $\alpha = 58.3^{\circ}$) and that a single epitaxy exists with the Si substrate such that α-GeTe(111)$\|$Si(111) and α-GeTe[$1\bar{1}0$]$\|$Si[$1\bar{1}0$] [23] in pseudocubic coordinates. We can also estimate the average azimuthal misorientation between grains to be $0.7^{\circ} \pm 0.2^{\circ}$ (Supplemental Material S1 in [35]). Moreover, as shown from the threefold symmetry of the 222_c Bragg peaks, the fraction of twinned grains is negligible in the layer. We estimate from the intensity of Bragg peaks that less than 5% of the layer contains twinned grains (less than 10% for the 60-nm-thick GeTe film).

In addition to the rhombohedral distortion of the GeTe unit cell, SHG microscopy combined to polarimetry analysis is a highly suited method to investigate the local symmetry and obtain the domain structure of noncentrosymmetric ferroic materials. This method is applied here to obtain the detailed domain structure of a 1800-nm-thick GeTe film. Figure 2(a) shows a SHG image revealing stripe domains superimposed to a background exhibiting a lower emission intensity. This image regroups all the domain contributions by combining three SHG images recorded at different sets of polarizer and analyzer angles as explained in the Supplemental Material S2 in [35]. The local SHG polarimetry confirms the $3m$ point group symmetry of the film and reveals an in-plane polarization at fine stripe domains superimposed to a background showing out-of-plane polarization (main c domain). The observation of the fine ferroelastic stripes is made possible by a convolution mechanism in SHG microscopy involving the focused laser (Gaussian) beam and the comparatively zero size of the nano-object like in the SHG imaging of domain walls [32]. This artificial broadening allows for the observation of the nanoscale domains and the spectral analysis of the their local emission (see the Supplemental Material, Fig. S3 [35]). The local polarization is derived through the precise modeling of the local SHG polarimetry (see Methods) and the result is displayed in the inset of Fig. 2(a). The GeTe(111) films show three stripe domains oriented in-plane at 90° and $\pm 30^{\circ}$ with respect to the x axis with a polarization oriented along the width of the stripes (see more details in the Supplemental Material, Figs. S4–S6 [35]).

As these ferroelastic nanodomains meet the surface of the film, they can be characterized by surface sensitive techniques, such as low energy electron microscopy (LEEM), with much higher resolution [39] [see Figs. 2(b) and 2(c)]. The LEEM contrast in reflectivity mode (bright field) shows bright and dark bands of intensity along the domains that reverse with the focusing conditions of the microscope [40] (see the Supplemental Material, Fig. S7 [35]). This is a typical feature of a ridge-and-valley morphology that indicates that the surface of the nanodomains is tilted. Tilted surface patterns are characteristic features of ferroelastic domains. The mean tilt angle of the nanodomains has been quantitatively characterized by μ-LEED [41]. The reflected beams from the three domains variants $(0, \pm 120^{\circ})$ are slightly off-specular with respect to the main $(0,0)$ reflected beam [Fig. 2(d) and inset of Fig. 2(e)] and the angular shift increases with the incident electron energy E [Fig. 2(e)]. Quantitatively the triangle area

A formed by the three equivalent reflected beams increases as

$$A = \frac{18}{\sqrt{3}} \frac{m}{\hbar^2} \pi \theta^2 E, \tag{1}$$

where θ is the tilt angle ($\theta \ll 1$), m is the electron mass, and $\hbar$ is the reduced Planck constant. These domains have a mean surface plane orientation that is tilted by $1.37^\circ \pm 0.03^\circ$ in the $\langle 11\bar{2} \rangle$ direction with respect to the average surface plane. These tilted planes make the same tilt angle as the (111) crystallographic planes of the a nanodomains obtained from the position of the minor Bragg peaks measured by x-ray diffraction. This unambiguously confirms the same ferroelastic origin of the nanodomains at the surface and in the bulk of the layer. From LEEM topographic measurements we have also quantified the evolution of the a-domain fraction α as a function of the film thickness [Fig. 1(d)]. Below 30 nm, the a-domain fraction is null and the film is therefore monodomain. Then it increases sublinearly [10,42] as $\alpha \sim [4.7 \pm 2.4] \times 10^{-3} h^{0.48 \pm 0.07}$ (h is the film thickness in nm). The domain width L [Fig. 1(d)] increases linearly over the entire range of thickness as $L \sim [0.043 \pm 0.005]h$ nm and reaches $\sim$77 nm for a 1825-nm-thick GeTe film. These LEEM measurements are also confirmed with the estimate of the a-nanodomain size from the full-width at half-maximum of the diffraction peaks of the minor domains [insets in Fig. 1(a)]. The domain fraction and domain size results allow us to evaluate the effective period $W = L/\alpha$ of the nanodomain pattern. It reaches $\sim$500 nm for a 1825-nm-thick GeTe film. Assuming in the mean strain approach [43–45] that

$$W = \frac{\sqrt{h_0 h}}{2\xi \alpha (1 - \alpha)}, \tag{2}$$

with $\xi = 0.27$, we have estimated a characteristic length $h_0 = 0.5 \pm 0.2$ nm of the nanodomain pattern that balances the gain of elastic energy and the costs of domain wall and interfacial stress with the substrate.

The atomic scale characterization of the 71°-type domain walls and a domains has been addressed by high-resolution transmission electron microscopy (HR-TEM [46]). Figure 3(a) shows an area including the Si substrate, an a domain and a c domain separated by a 71°-type domain wall. Strain and rotation mapping of the crystalline lattice of the GeTe layer in this area can be determined by comparison with a reference (unstrained) region of the Si substrate far from the interface. This has been carried out using the GPA image-processing technique [5,47,48]. Considering that the x and y axes are, respectively, parallel and perpendicular to the domain wall, we evidence that the diagonal components of the strain tensor ϵ_{xx} and ϵ_{yy} are equal on both sides of the wall, whereas the pure shear component ϵ_{xy} and rotation field ω_{xy} make a significant jump across the domain wall [Fig. 3(b)]. One can notice that shear and rotation (2.2°) components compensate across the wall to have a coplanar (110) plane as expected from mechanical compatibility of the interface between a and c domains [Fig. 3(c)] [49].

Ferroelastic nanodomain formation and ferroelectric switching processes are known to be highly sensitive to the mechanical interactions with the substrate due to the stress induced by the lattice mismatch. This effect may be even more pronounced for epitaxial films. To address the relaxation

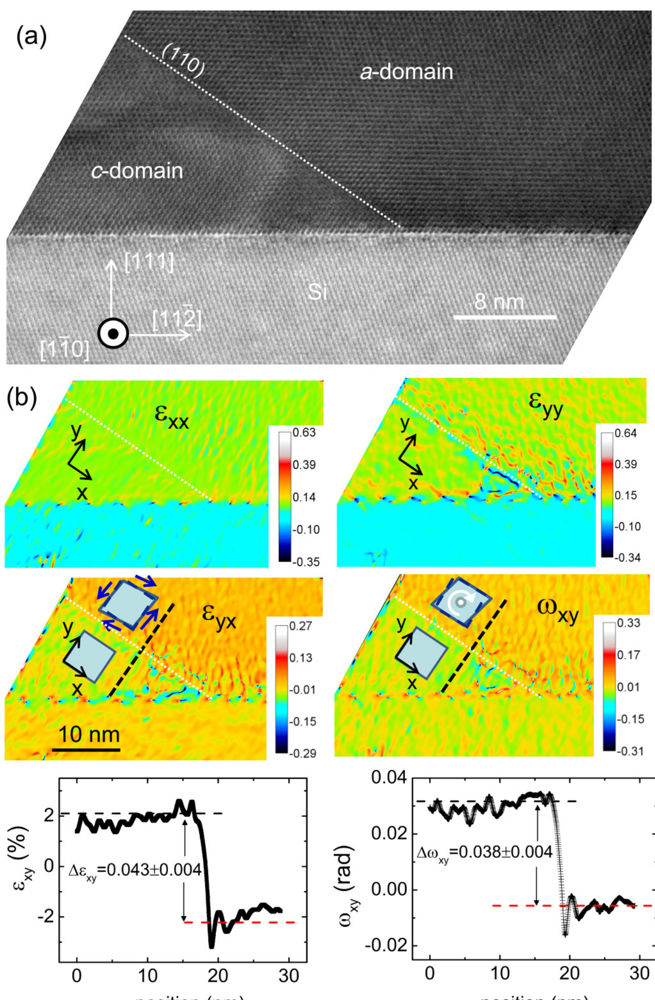

FIG. 3. (a) HR-TEM cross section ($\langle 1\bar{1}0 \rangle$ zone axis) of the interfacial area between the Si substrate, a GeTe c domain, and an a nanodomain (domain wall: Dotted white line) for a 460-nm-thick GeTe film. (b) In-plane ϵ_{xx}, out-of-plane ϵ_{yy}, shear ϵ_{xy} strain, and rotation ω_{xy} with x and y, respectively, parallel and perpendicular to the domain wall. (c) Line profiles of shear and rotation across the wall [see dark dashed line in (b)].

mechanisms prevailing in the formation of these ferroelastic nanodomains, we have characterized the GeTe/Si interface with HR-TEM. Figure 4(a) shows the in-plane strain field (ϵ_{xx}) across the interface with x along $\langle 11\bar{2} \rangle$. The lattice parameter mismatch between the Si substrate and the GeTe c domain is locally $8.2 \pm 0.2\%$ [Fig. 4(c)]. In the a nanodomain ϵ_{xx} is larger ($12.2 \pm 0.2\%$) due to the nearly in-plane stretch of the rhombohedral distortion. Considering the lattice mismatch, the formation of a domains is elastically unfavorable if the in-plane lattice deformation is fixed by the Si substrate lattice parameter. However, the regular modulation of the in-plane strain component ϵ_{xx} in GPA analysis shows that this huge lattice parameter mismatch between the Si substrate and GeTe thin film is relaxed via interfacial misfit dislocations with a period of 4.10 nm (2.77 nm) for the c domain (a domain). This result shows that the dislocation-assisted stress release is the main relaxation mechanism of the interface [see Fig. 4(b)]. To compare the interfacial energy cost of both GeTe c domains

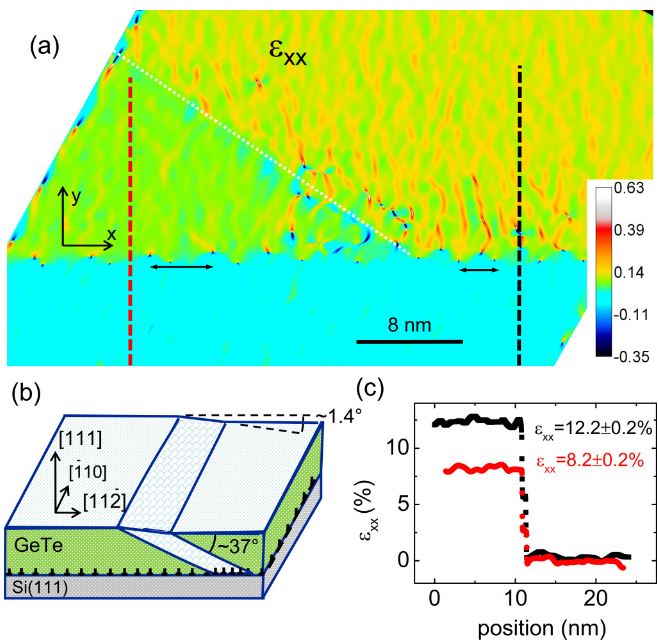

FIG. 4. (a) In-plane strain ϵ_{xx} with x along the $\langle 11\bar{2}\rangle$ GeTe/Si interface obtained from GPA analysis. The arrows at the GeTe/Si interface show the regular modulation of ϵ_{xx}. (b) Model of the internal structure of GeTe thin films on Si(111). (c) Line profiles of in-plane strain ϵ_{xx} across the interface [see dashed line in (a): dark (red) line across the a domain (c domain)].

and a domains we can make some preliminary remarks. (i) The linear density of misfit dislocations is higher for the a domains (0.36 nm^{-1}) than for the c domains (0.24 nm^{-1}). (ii) The in-plane lattice of the a nanodomains is monoclinic, whereas it is hexagonal for the GeTe c domains (as for the Si substrate). (iii) At last the interface plane of the a nanodomains is expected to be tilted by 1.36° with respect to the Si surface plane [tilt angle of (111) plane], whereas the main GeTe c domain and Si substrate are coplanar. Therefore, the formation of the a nanodomains appears to be energetically unfavorable.

To address the metastability of these a nanodomains, we have performed LEEM measurements during heating and cooling thermal treatments of GeTe thin films (see the Supplemental Material, Fig. S8 [35] and corresponding movie). Figure 5 shows that the ferroelastic nanodomains disappear at ∼250 °C, i.e., slightly below the growth temperature (275 °C) while the thin film remains in its rhombohedral α phase. This is far below the Curie temperature of GeTe that is around 400 °C [50,51]. Therefore, we assume that a ferroelastic configuration with only a single domain occurs during GeTe growth with a unique rhombohedral distortion perpendicular to the film. When cooling, the ferroelastic a nanodomains nucleate abruptly at 210 ± 10 °C. This process is perfectly reproducible cycling the temperature. To explain this behavior we infer that upon cooling a thermal stress arises due to the different linear thermal expansion coefficients of GeTe [50,52] $\sim 31.9 \times 10^{-6}\ \text{K}^{-1}$ and Si [53,54] $\sim 3.5 \times 10^{-6}\ \text{K}^{-1}$. Assuming that the interfacial misfit dislocations are not mobile enough to accommodate this change [55–58] and given that the GeTe lattice parameter should decrease faster

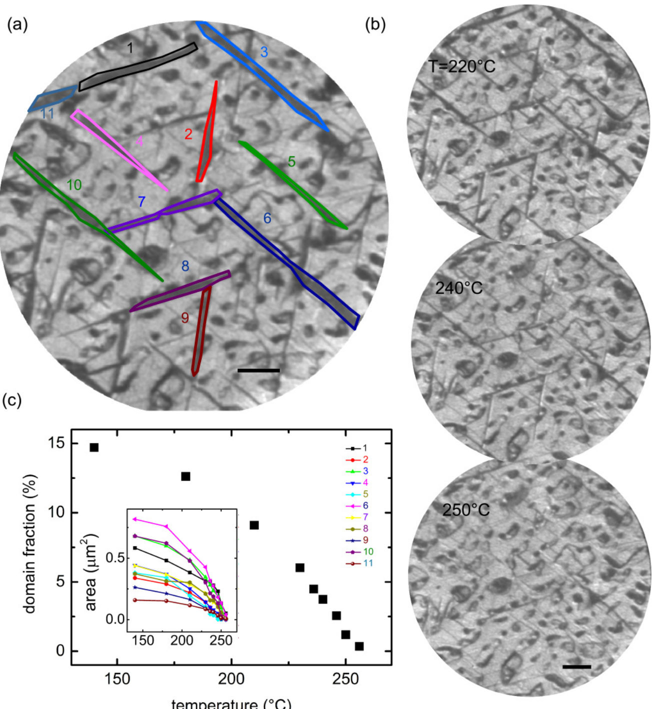

FIG. 5. (a) LEEM image (bright field mode excluding the reflected beam from the nanodomains) of GeTe thin film (1455 nm) at 180 °C. (b) Series of LEEM images at 220, 240, and 250 °C. Scale bar 1 μm. (c) Temperature evolution of a nanodomains fraction as a function of temperature [inset: temperature evolution of some domains area shown in (a)]. The dark contrast areas that do not have a needle shape correspond to local depressions in the GeTe thin film.

than that of Si substrate, a tensile in-plane strain occurs in the GeTe layer. A very efficient way to macroscopically reduce this stress is to nucleate a domains that expand locally the in-plane lattice parameter in the $\langle 11\bar{2}\rangle$ direction. The three variants of the ferroelastic domains provide a global isotropic relaxation. When the GeTe layer is annealed at a temperature close to the growth temperature, it recovers its growth lattice parameter, and therefore the a nanodomains are elastically useless and spontaneously decay [see Figs. 5(b) and 5(c)]. The hysteretic behavior of the a domains indicates also that a nucleation energy barrier must be overpassed for their formation.

IV. CONCLUSION

In conclusion, the domain structure of α-GeTe thin films epitaxially grown on Si(111) has been investigated. By combining 3D reciprocal space mapping by x-ray diffraction, HR-TEM, SHG, and LEEM, we have quantified the volume fraction and size of the nanodomains as a function of the film thickness. We have demonstrated that domain walls are only of 71° type and the interface with the Si substrate is stabilized by misfit dislocations that relaxes the large lattice parameter mismatch. Using *in situ* LEEM under cooling we have shown that the ferroelectric a nanodomains nucleate and grow, whereas they decay under annealing and disappear at 250 °C. This result indicates that during GeTe growth at 275 °C, a single domain configuration occurs with a polarization perpendicular to the film surface. We infer that this single

domain state during growth is a key parameter that favors the high crystalline quality of the GeTe layer. Then the driving force for the formation of the ferroelectric nanodomains at lower temperature is attributed to the thermal stress as the dislocations are frozen and cannot accommodate the relative change of the lattice parameter. We believe that this detailed description of domain behavior as a function of temperature and film thickness will serve as a playground for the control of ferroelectric/ferroelastic nanodomains in GeTe and will motivate new strategies to tune the Rashba effect by addressing the motion of domain walls.

ACKNOWLEDGMENTS

The project leading to this publication has received funding from Excellence Initiative of Aix-Marseille University A*MIDEX, a french "Investissements d'Avenir" programme through the AMUtech Institute. This work has also been supported by the ANR Grants HOLOLEEM (ANR-15-CE09-0012) and TOPELEC (ANR-18-CE92-0052). S.C.-H. and C.V. acknowledge funding by the LabEx NIE (ANR-11-LABX-0058-NIE) in the framework of the Interdisciplinary Thematic Institute QMat (ANR-17-EURE-0024), as part of the ITI 2021-2028 program supported by the IdEx Unistra (ANR-10-IDEX-0002-002) and SFRI STRATUS (ANR-20-SFRI-0012) through the French Programme d'Investissement d'Avenir. The authors acknowledge the assistance of O. Grégut during SHG measurements and insightful discussion about symmetry aspects with U. Acevedo-Salas. We are grateful to Martiane Cabié (CP2M, Marseille) for lamella preparation of GeTe thin films by Focused Ion Beam.

[1] N. A. Pertsev, A. G. Zembilgotov, and A. K. Tagantsev, Phys. Rev. Lett. **80**, 1988 (1998).
[2] M. Dawber, K. M. Rabe, and J. F. Scott, Rev. Mod. Phys. **77**, 1083 (2005).
[3] J. M. Gregg, Phys. Status Solidi A **206**, 577 (2009).
[4] G. Catalan, A. Janssens, G. Rispens, S. Csiszar, O. Seeck, G. Rijnders, D. H. A. Blank, and B. Noheda, Phys. Rev. Lett. **96**, 127602 (2006).
[5] G. Catalan, A. Lubk, A. H. G. Vlooswijk, E. Snoeck, C. Magen, A. Janssens, G. Rispens, G. Rijnders, D. H. A. Blank, and B. Noheda, Nat. Mater. **10**, 963 (2011).
[6] T. Yamada, D. Ito, T. Sluka, O. Sakata, H. Tanaka, H. Funakubo, T. Namazu, N. Wakiya, M. Yoshino, T. Nagasaki, and N. Setter, Sci. Rep. **7**, 5236 (2017).
[7] A. K. Yadav, C. T. Nelson, S. L. Hsu, Z. Hong, J. D. Clarkson, C. M. Schlepueetz, A. R. Damodaran, P. Shafer, E. Arenholz, L. R. Dedon, D. Chen, A. Vishwanath, A. M. Minor, L. Q. Chen, J. F. Scott, L. W. Martin, and R. Ramesh, Nature (London) **530**, 198 (2016).
[8] M. Hadjimichael, Y. Li, E. Zatterin, G. A. Chahine, M. Conroy, K. Moore, E. N. O' Connell, P. Ondrejkovic, P. Marton, J. Hlinka, U. Bangert, S. Leake, and P. Zubko, Nat. Mater. **20**, 495 (2021).
[9] E. K. H. Salje, J. Appl. Phys. **128**, 164104 (2020).
[10] V. Nagarajan, I. G. Jenkins, S. P. Alpay, H. Li, S. Aggarwal, L. Salamanca-Riba, A. L. Roytburd, and R. Ramesh, J. Appl. Phys. **86**, 595 (1999).
[11] A. H. G. Vlooswijk, B. Noheda, G. Catalan, A. Janssens, B. Barcones, G. Rijnders, D. H. A. Blank, S. Venkatesan, B. Kooi, and J. T. M. De Hosson, Appl. Phys. Lett. **91**, 112901 (2007).
[12] L. Feigl, L. J. McGilly, C. S. Sandu, and N. Setter, Appl. Phys. Lett. **104**, 172904 (2014).
[13] D. Di Sante, P. Barone, R. Bertacco, and S. Picozzi, Adv. Mater. **25**, 509 (2013).
[14] M. Liebmann, C. Rinaldi, D. Di Sante, J. Kellner, C. Pauly, R. N. Wang, J. E. Boschker, A. Giussani, S. Bertoli, M. Cantoni, L. Baldrati, M. Asa, I. Vobornik, G. Panaccione, D. Marchenko, J. Sanchez-Barriga, O. Rader, R. Calarco, S. Picozzi, R. Bertacco, and M. Morgenstern, Adv. Mater. **28**, 560 (2016).
[15] C. Rinaldi, S. Varotto, M. Asa, J. Slawinska, J. Fujii, G. Vinai, S. Cecchi, D. Di Sante, R. Calarco, I. Vobornik, G. Panaccione, S. Picozzi, and R. Bertacco, Nano Lett. **18**, 2751 (2018).
[16] J. Krempasky, S. Muff, J. Minar, N. Pilet, M. Fanciulli, A. P. Weber, E. B. Guedes, M. Caputo, E. Muller, V. V. Volobuev, M. Gmitra, C. A. F. Vaz, V Scagnoli, G. Springholz, and J. H. Dil, Phys. Rev. X **8**, 021067 (2018).
[17] C. Rinaldi, J. C. Rojas-Sanchez, R. N. Wang, Y. Fu, S. Oyarzun, L. Vila, S. Bertoli, M. Asa, L. Baldrati, M. Cantoni, J. M. George, R. Calarco, A. Fert, and R. Bertacco, APL Mater. **4**, 032501 (2016).
[18] J. Slawinska, D. Di Sante, S. Varotto, C. Rinaldi, R. Bertacco, and S. Picozzi, Phys. Rev. B **99**, 075306 (2019).
[19] Y. Li, Y. Li, P. Li, B. Fang, X. Yang, Y. Wen, D.-X. Zheng, C.-H. Zhang, X. He, A. Manchon, Z.-H. Cheng, and X.-x. Zhang, Nat. Commun. **12**, 540 (2021).
[20] H. S. Lee, B.-S. Kim, C.-W. Cho, M.-W. Oh, B.-K. Min, S.-D. Park, and H.-W. Lee, Acta Mater. **91**, 83 (2015).
[21] P. A. Vermeulen, A. Kumar, G. H. ten Brink, G. R. Blake, and B. J. Kooi, Cryst. Growth Des. **16**, 5915 (2016).
[22] A. V. Kolobov, D. J. Kim, A. Giussani, P. Fons, J. Tominaga, R. Calarco, and A. Gruverman, APL Mater. **2**, 066101 (2014).
[23] R. Wang, J. E. Boschker, E. Bruyer, D. Di Sante, S. Picozzi, K. Perumal, A. Giussani, H. Riechert, and R. Calarco, J. Phys. Chem. C **118**, 29724 (2014).
[24] D. Kriegner, G. Springholz, C. Richter, N. Filet, E. Mueller, M. Capron, He. Berger, V. Holy, J. H. Dil, and J. Krempasky, Crystals **9**, 335 (2019).
[25] S. Picozzi, Front. Phys. **2**, 10 (2014).
[26] S. Picozzi, *Multiferroic and Ferroelectric Rashba Semiconductors* (Springer International, Cham, 2020), pp. 375–400.
[27] S. Andrieu, J. Appl. Phys. **69**, 1366 (1991).
[28] C. Mocuta, M.-I. Richard, J. Fouet, S. Stanescu, A. Barbier, C. Guichet, O. Thomas, S. Hustache, A. V. Zozulya, and D. Thiaudiere, J. Appl. Crystallogr. **46**, 1842 (2013).
[29] S. A. Denev, T. T. A. Lummen, E. Barnes, A. Kumar, and V. Gopalan, J. Am. Ceram. Soc. **94**, 2699 (2011).
[30] S. Cherifi-Hertel, He. Bulou, R. Hertel, G. Taupier, K. D. (Honorat) Dorkenoo, C. Andreas, J. Guyonnet, I. Gaponenko, K. Gallo, and P. Paruch, Nat. Commun. **8**, 15768 (2017).

[31] H. Yokota and Y. Uesu, J. Appl. Phys. **129**, 014101 (2021).
[32] S. Cherifi-Hertel, C. Voulot, U. Acevedo-Salas, Y. Zhang, O. Crégut, K. D. Dorkenoo, and R. Hertel, J. Appl. Phys. **129**, 081101 (2021).
[33] K. J. Spychala, P. Mackwitz, A. Widhalm, G. Berth, and A. Zrenner, J. Appl. Phys. **127**, 023103 (2020).
[34] K. J. Spychala, P. Mackwitz, M. Ruesing, A. Widhalm, G. Berth, C. Silberhorn, and A. Zrenner, J. Appl. Phys. **128**, 234102 (2020).
[35] See Supplemental Material at http://link.aps.org/supplemental/10.1103/PhysRevMaterials.5.124415 for x-ray diffraction measurements, SHG images and polarimetry analysis, as well as LEEM data.
[36] Y. Zhang and S. Cherifi-Hertel, Opt. Mater. Express **11**, 3736 (2021).
[37] Z. L. Luo, H. Huang, H. Zhou, Z. H. Chen, Y. Yang, L. Wu, C. Zhu, H. Wang, M. Yang, S. Hu, H. Wen, X. Zhang, Z. Zhang, L. Chen, D. D. Fong, and C. Gao, Appl. Phys. Lett. **104**, 182901 (2014).
[38] J. Chrosch and E. K. H. Salje, J. Appl. Phys. **85**, 722 (1999).
[39] N. Barrett, J. E. Rault, J. L. Wang, C. Mathieu, A. Locatelli, T. O. Mentes, M. A. Niño, S. Fusil, M. Bibes, A. Barthélémy, D. Sando, W. Ren, S. Prosandeev, L. Bellaiche, B. Vilquin, A. Petraru, I. P. Krug, and C. M. Schneider, J. Appl. Phys. **113**, 187217 (2013).
[40] K. M. Yu, A. Locatelli, and M. S. Altman, Ultramicroscopy **183**, 109 (2017).
[41] W. X. Tang, K. L. Man, H. C. Huang, C. H. Woo, and M. S. Altman, J. Vac. Sci. Technol. B **20**, 2492 (2002).
[42] W. Y. Hsu and R. Raj, Appl. Phys. Lett. **67**, 792 (1995).
[43] A. L. Roytburd, J. Appl. Phys. **83**, 228 (1998).
[44] A. L. Roytburd, J. Appl. Phys. **83**, 239 (1998).
[45] A. K. Tagantsev, L. E. Cross, and J. Fousek, *Domains in Ferroic Crystals and Thin Films* (2010), pp. 1–821.
[46] E. Snoeck, A. Lubk, and C. Magén, *Structural Characterization of Ferroelectric and Multiferroic Nanostructures by Advanced TEM Techniques* (John Wiley & Sons, New York, 2016), Chap. 10, pp. 275–324.
[47] M. J. Hytch, E. Snoeck, and R. Kilaas, Ultramicroscopy **74**, 131 (1998).
[48] J.-L. Rouvière and E. Sarigiannidou, Ultramicroscopy **106**, 1 (2005).
[49] J. Fousek and V. Janovec, J. Appl. Phys. **40**, 135 (1969).
[50] T. Chattopadhyay, J. X. Boucherle, and H. G. Vonschnering, J. Phys. C Solid State **20**, 1431 (1987).
[51] A. Schlieper, Y. Feutelais, S. G. Fries, B. Legendre, and R. Blachnik, Calphad **23**, 1 (1999).
[52] M. Gallard, M. Salah Amara, M. Putero, N. Burle, C. Guichet, S. Escoubas, M.-I. Richard, C. Mocuta, R. R. Chahine, M. Bernard, P. Kowalczyk, P. Noe, and O. Thomas, Acta Mater. **191**, 60 (2020).
[53] R. R. Reeber and K. Wang, Mater. Chem. Phys. **46**, 259 (1996).
[54] H. Watanabe, N. Yamada, and M. Okaji, Int. J. Thermophys. **25**, 221 (2004).
[55] N. A. Pertsev and A. G. Zembilgotov, J. Appl. Phys. **80**, 6401 (1996).
[56] K. S. Lee and S. Baik, J. Appl. Phys. **85**, 1995 (1999).
[57] K. Lee, K. S. Lee, and S. Baik, J. Appl. Phys. **90**, 6327 (2001).
[58] K. S. Lee, J. H. Choi, J. Y. Lee, and S. Baik, J. Appl. Phys. **90**, 4095 (2001).